Systematics of angular-dependent neutron production by 585 MeV protons on targets with $12 \leq A \leq 238$: Differential cross section measurements

S. Cierjacks, Y. Hino,* F. Raupp, and L. Buth†
Kernforschungszentrum Karlsruhe, Institut für Kernphysik, D-7500 Karlsruhe, Federal Republic of Germany

D. Filges, P. Cloth, and T. W. Armstrong
Institut für Reaktorentwicklung, Kernforschungsanlage Jülich, D-5170 Jülich, Federal Republic of Germany
(Received 19 January 1987)

Double differential cross sections $d^2\sigma/d\Omega dT_n$ for the production of neutrons from 585 MeV proton bombardment of C, Al, Fe, Nb, In, Ta, Pb, and U targets have been measured at emission angles of 30°, 90°, and 150° and for neutron kinetic energies between 0.9 and 585 MeV (all quantities in the laboratory system). The measured cross sections are compared with previous experimental results from other laboratories. The experimental energy-dependent cross sections all reveal a clear two-component structure with contributions from evaporation processes and intranuclear cascade reactions. For heavy and medium weight target nuclei the data in the evaporation region are indicative of an isotropic angular distribution in the zero linear momentum coordinate system. Data in the cascade energy region are strongly forward peaked, and the fraction of cascade neutrons increases with decreasing emission angle. This fraction also increases with decreasing mass number.

I. INTRODUCTION

The systematic studies described in this paper were performed as part of a study project for a new spallation neutron source (SNQ).[1] They followed the measurements of thick sample yields and spectra[2] (in the initial phase of our program) which were more closely related to design and operation considerations for a suitable SNQ target. Differential cross sections measured over a broad range of target masses, emission angles, and secondary energies are also well suited to provide a better physical understanding of the spallation process. In order to predict the important quantities, such as differential production cross sections, secondary particle yields, and spectra, etc. produced in the interactions of high-energy protons with complex nuclei, various approaches for theoretical calculations have been made in the past.[3–7] However, all of these calculations are based on models which involve assumptions that cannot be fully justified theoretically. Therefore, additional justification relies still on detailed comparisons of theoretical predictions with precise measurements. Above the pion-production threshold the majority of existing experimental data for such comparison comes from measurements of secondary protons emitted in the range from 0° to 60°.[8,9] For these data it has been proven[6] that there is reasonable agreement between experiments and predictions from the intranuclear cascade-evaporation model. In contrast to proton data, secondary neutron measurements at incident proton energies above 200 MeV are rather scarce. Furthermore, such results are, with a few exceptions,[10,11] limited to 0° (Refs. 12–14) or to small emission angles,[10] and special thick-sample neutron yields and spectra.[15–17]

Analysis of some of the latter results[15,16] indicated that the thick-sample neutron yields predicted by the intranuclear cascade model are too small for emission angles $\gtrsim 45°$. Moreover, it was found that the discrepancy between theory and experiment increases with increasing emission angle. For incident proton energies below 200 MeV, Wachter *et al.*[18] reported a similar discrepancy also in the 135° neutron production cross sections of carbon and aluminum. On this basis, the main purpose of the present work was to investigate in more detail the discrepancies between calculations and measurements of neutron production cross sections. Such extended data provide a good means of validating theoretical assumptions or particular choices of model parameters. Since the incident proton energy in our experiments is well above the meson-production threshold, the data are also of particular value for comparisons with model calculations including meson production and its effects on high-energy neutron production.

In Sec. II we discuss the experimental details of the measurements. On-line data accumulation is outlined in Sec. III. The off-line data analysis is described in Sec. IV. The results of the measurements are presented and discussed in Sec. V. In the following paper,[19] the present experimental results are compared with theoretical predictions from the intranuclear cascade-evaporation model.[20]

II. EXPERIMENTAL DETAILS

A. Method

Differential cross section measurements were performed by the time-of-flight method employing the micropulse structure of the Schweizerisches Institut für Nuklearforschung (SIN) cyclotron beam. During all

measurements the cyclotron was run in a special operation mode providing microstructure pulses at a reduced pulse repetition frequency of 16.9 MHz with a standard pulse width of ≤ 200 ps. For secondary neutron detection simultaneously over the whole energy range 0.9–585 MeV, a proton-recoil scintillation counter was employed and used for n-γ pulse shape discrimination (PSD).[21] For measurements of absolute cross sections the neutron detection efficiency of the scintillation counter was determined to an accuracy of $\leq 10\%$ by associated-particle measurements[22] and Monte Carlo calculations (see Sec. IV). Charged-particle contamination in the incident neutron beam was removed from on-line data accumulation by using a thin plastic scintillator in front of the neutron counter and operating both detectors in the veto mode (the passage of charged particles typically causes both detectors to generate a signal). For standard cross section measurements a highly collimated neutron beam was used.

B. Proton beam

The experiments were performed in the pM1 channel of the SIN facility. In this channel protons are provided by scattering the extracted beam of the cyclotron in an 8 mm thick beryllium target through an angle of 8°. The kinetic energy of the proton beam was 585 MeV with an absolute calibration uncertainty of 2 MeV (one standard deviation) and an energy spread of 2.34 MeV full width at half maximum (FWHM).[23] The beam intensity during the measurements was typically of the order of a few 10^9 p/s. The position and the profile of the beam in front of and behind the target position was monitored throughout all measurements by means of two analog-readout multiwire proportional chambers.[24] With these we determined the extensions of the beam spot at the target position as typically 10 mm (FWHM) in the vertical direction and 15 mm (FWHM) in the horizontal direction. The proton flux was also monitored throughout the experiments using a scintillation counter telescope which detected charged particles scattered at $\sim 35°$ to the incident proton beam direction from a 5 mm polyethylene scatterer placed in the proton beam far upstream of the neutron producing target. For the telescope counters, two NE102A (Nuclear Enterprises Corp., Edinburgh, Scotland) plastic scintillators (both 5 mm thick) were chosen, and operated in coincidence. The telescope counter was calibrated to absolute proton flux by counting individual protons in the direct beam at extremely reduced currents, employing an additional plastic scintillation counter in special auxiliary calibration runs. For this purpose a reduction in proton beam intensity by more than three orders of magnitude was achieved by detuning a quadrupole magnet upstream of the acceptance-defining slit system of the pM1 beam line.[23] By this procedure the beam intensity could be reduced without changing the beam dimensions at the position of the proton target. A direct measurement of the proton flux could then be made with a 10×10 cm^2, 5 mm thick plastic scintillator placed at the target position, and its count rate related to the telescope coincidence rate. Such calibrations were carried out several times during the runs and gave consistent results within the statistical uncertainties of the individual measurements. Flux calibrations of the above type were performed at count rates between 2×10^5 and 1×10^6 p/s in the direct counter, and thus required 5–15% corrections for dead time losses.

C. Target-detector arrangement

Figure 1 is a schematic drawing of the target-detector arrangement. The incident proton beam after passing through about 5 m of air was well focused to the center of the thin metal targets. As the proton targets, 10 cm square plates a few millimeters thick were used, except uranium. In this case a 5×10 cm^2 plate of natural uranium cladded in 12 μm of Ni was chosen and placed into the beam with the 10 cm dimension in the horizontal direction. The targets all consisted of high-purity elements in their natural isotopic composition.

For all targets both the thickness and the density were measured separately with an overall accuracy of $\leq 2\%$. In Table I the essential physical properties of the target materials used in the present measurements are summarized. These include target thicknesses, chemical purities, and energy losses of 585 MeV protons in the target. While in the measurements at laboratory angles of 30° and 150° the target plates were adjusted with their planes perpendicular to the proton beam axis, the plates were turned around in the 90° measurements so that their normal to the target included an angle of 45° with the incident beam direction. For this reason the measurements at 90° involved $\sqrt{2}$ times larger effective target thicknesses than those listed in Table I. Highly collimated neutron beams at angles of 30°, 90°, and 150° were provided by 4 cm diam beam holes in the 20 cm high steel collimators assembled to the shape shown in Fig. 1 and reinforced with heavy concrete all around the

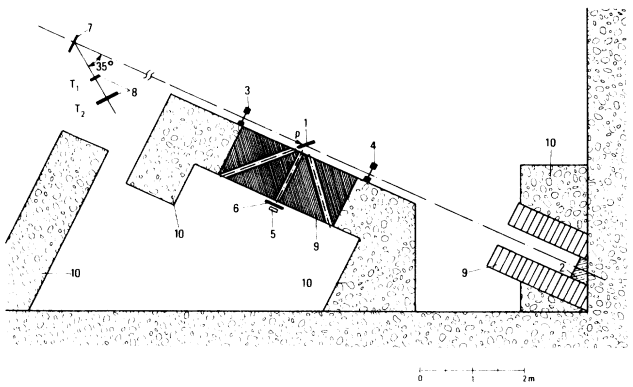

FIG. 1. Schematic drawing of the target-detector arrangement at the SIN cyclotron. (1) Target in position for the 90° measurement, (2) proton beam stop, (3),(4) multiwire proportional chambers for beam profile measurements, (5) main neutron counter, (6) veto counter, (7) CH_2 scatterer, (8) monitor telescope counters, (9) iron shielding, and (10) heavy concrete shielding.

TABLE I. Properties of proton targets.

Target	Thickness (mm)	Thickness (g/cm^2)	Chemical purity (at. %)	Energy loss[a] (MeV)
C	5.40	1.19	99.99	2.7
Al	5.58	1.51	99.96	3.1
Fe	3.93	3.09	99.85	5.8
Nb	4.00	3.43	99.9	5.6
In	5.13	3.75	99.95	6.1
Ta	5.40	8.99	99.8	12.5
Pb	4.40	4.99	99.99	6.8
U[b]	3.14	5.95	99.7	7.8

[a]Energy loss of 585 MeV protons in the target.
[b]Cladded in 12 μm of nickel.

iron shield. The principal neutron detector was a 3 cm thick, 4.5 cm diam NE213 liquid scintillator, with a thin (3 mm), 8 cm diam NE102A plastic scintillator placed as the veto counter ~ 5 cm in front of it. Standard background determinations were performed with the target plates opposite the collimator entrance removed. From auxiliary measurements with the target plates left in the irradiation position, but iron plugs inserted into the collimator holes over their total length, it has been verified that neutron transmission through the shielding was small ($\lesssim 1\%$ even for the highest energies). But both types of background measurements are not sensitive to possible background effects from small angle scattering on the inner walls of the iron collimators. The influence of this kind of background effects was studied in a complementary so-called "open geometry" run at 90°. In this case only the beam dump of the direct proton beam was heavily shielded. Foreground measurements were then performed without any shielding between the target and the detector. In the corresponding background runs an iron shadow rod, 6 cm in diameter and 1.5 m long, was inserted between the target and the neutron counter.

Measurements of the differential neutron production cross sections involving the "open geometry" setup were performed for all eight targets at this emission angle. A comparison of these results with the results from standard measurements showed a good overall agreement over the total range of the emission spectra. A typical example of these comparisons is shown in Fig. 2, which illustrates the results for iron. This type of comparison gave additional confidence that background effects from small angle scattering in the collimator walls were small, and could be neglected. This result was also confirmed from Monte Carlo computer simulations of our experimental setup.[25]

D. Time-of-flight measurements

Spectrum measurements over the secondary neutron energy range from 0.9 to 585 MeV were performed over a flight path of ~ 1.3 m for all three laboratory angles of 30°, 90°, and 150°. A typical unfolded time-of-flight spectrum is shown in Fig. 3. The auxiliary "open geometry" measurements at 90° (see Sec. II C) involving a flight path of 1.7 m covered the neutron energy range from 1.2 to 585 MeV. In the standard measurements a total flight path uncertainty $\Delta l = 3.05$ cm resulted from a quadrature effect of a 3 cm scintillator thickness and a

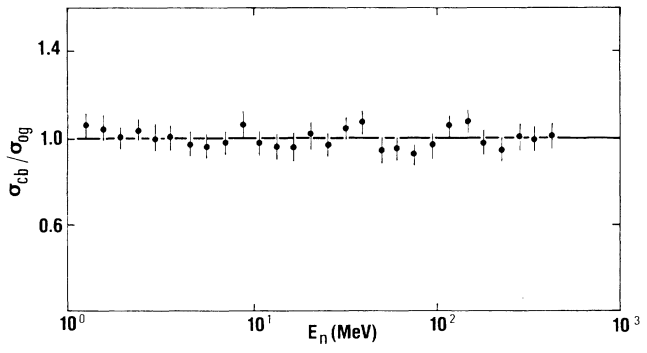

FIG. 2. Ratio of cross section measurements for iron employing a highly collimated neutron beam, σ_{cb}, and using an "open geometry" setup, σ_{og} (see text). It can be seen that both experimental methods provide, within the stated uncertainties, the same absolute results.

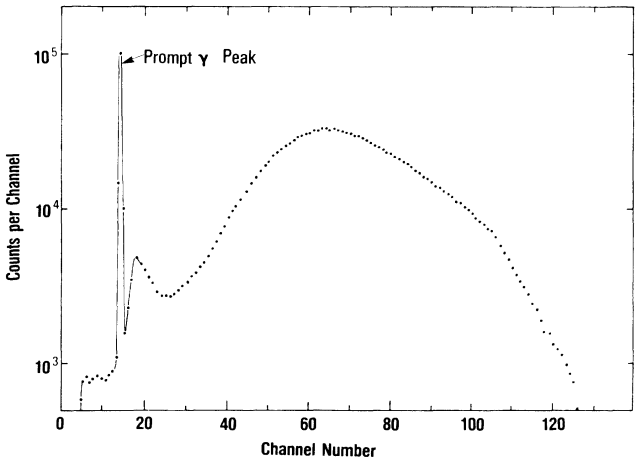

FIG. 3. Time-of-flight spectrum from bombardment of a thin lead target with 585 MeV protons. The original data are unfolded with respect to a single overlap in time (see Sec. IV). Time separation was accomplished by use of the two-dimensional array of pulse height vs flight time.

~ 0.5 cm target thickness. In addition, a total time uncertainty $\Delta t = 0.5$ ns (FWHM) was achieved for proton recoil energies above ~ 2 MeV in all measurements. This value results from the quadrature sum of the total detector time uncertainty (450 ps), the proton pulse duration (≤ 200 ps), and the dispersion of the reference timing signal (100 ps). The above timing specifications have been measured in auxiliary calibration runs. While the timing properties of the neutron detector were determined from coincidence measurements with a ^{60}Co γ source against a fast test detector (NE111 coupled to an XP2020 Valvo photomultiplier), the proton pulse duration on the target was measured by employing the prompt γ peak from the neutron producing target. (The upper limit of 200 ps is due to the timing resolution of the test detector.) Employing the experimental uncertainties in total time and flight path uncertainty allowed us to calculate the achieved fractional energy resolution by the approximate equation

$$\Delta T/T = \gamma(\gamma+1)[(\Delta l/l)^2 + (\Delta t/t)^2]^{1/2} , \quad (1)$$

where γ is the Lorentz contraction factor, and l and t are the flight path length and the neutron flight time, respectively. The corresponding energy resolutions achieved in the measurements are listed in Table II for a few typical neutron energies.

TABLE II. Typical energy resolutions vs energy achieved in the present time-of-flight measurements.

E_n (MeV)	t_n[a] (ns)	$\Delta T/T$[b] (%)
1	94.06	2.5
5	42.20	3.3
10	29.96	4.1
50	13.82	8.0
100	10.13	11.5
300	6.65	23.0
500	5.72	33.8

[a]Flight time of neutrons for a 1.3 m flight path.
[b]Calculated from Eq. (1).

III. DATA ACCUMULATION

Data accumulation was accomplished with a four-parameter setup. A simplified circuit diagram of the electronics used for data recording is shown schematically in Fig. 4. The pulse height signal from the liquid scintillator was split and fed through two fast amplifer channels, one with 10 times the gain of the other. This split was necessary to cover the wide dynamic range together with the expanded threshold region (a precise measurement of the effective detector threshold was an important prerequisite for an accurate determination of the neutron detection efficiency). The timing signal from the liquid scintillator was involved in the three functions:

(i) It started the main time-to-analog converter (TAC) which provided the neutron time-of-flight information via analog-to-digital convertor (ADC4). This TAC is stopped by a timing reference signal derived from the cyclotron radio frequency.

(ii) In conjunction with the timing signal from the

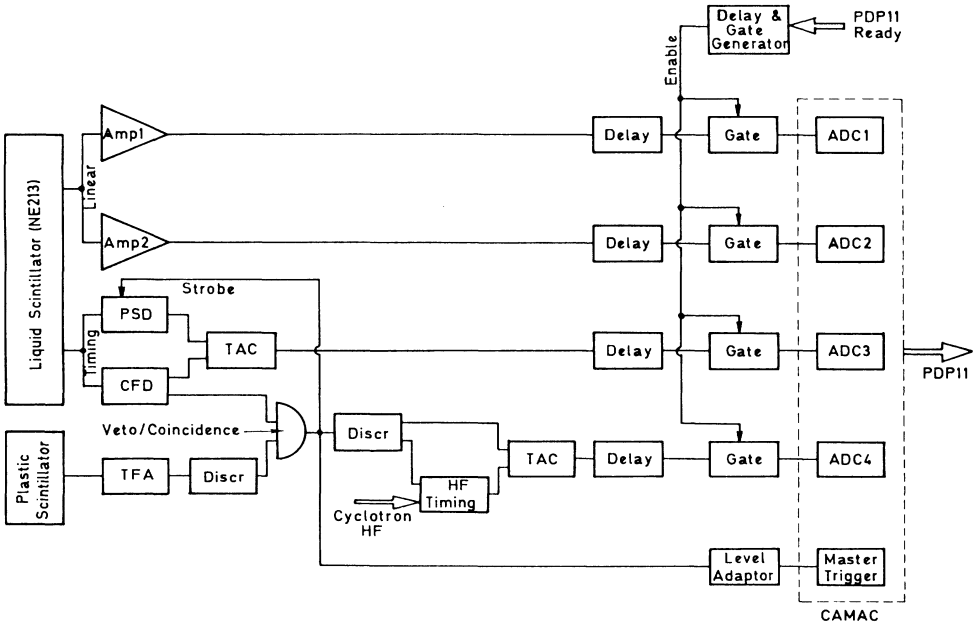

FIG. 4. Simplified circuit diagram of the electronics used in the present experiments. For data accumulation a four-parameter setup was used to record the neutron time of flight, the secondary charged-particle energy in two separate amplifier channels (one with 10 times the gain of the other), and a "pulse-shape discrimination" time.

plastic scintillator, it was used to operate a coincidence circuit in the veto mode, to generate a master trigger signal which notified the computer that an event of interest had occurred and the gates to the ADC's should be opened.

(iii) It provided the input signal for the n-γ pulse-shape discriminator. The result of this analysis appeared as a "PSD time signal" from the time-to-analog converter (TAC 2) the output of which went to ADC 3.

The contents of the four ADC's were stored event by event on magnetic tape for subsequent off-line data analysis. The number of master triggers applied to the computer was recorded and used in conjunction with the number of accepted events, to evaluate the dead time corrections.

For accurate determinations of the neutron detector thresholds applied in the measurements, auxiliary calibration runs were carried out at several times during an experimental period. These threshold determinations involved gamma rays from ^{137}Cs, ^{60}Co, ^{22}Na, and Am-Be sources in terms of the electron energy of the corresponding Compton edges between 0.5 and 4.2 MeV_{ee}. Least-squares fits of electron energy versus channel number resulted in $\leq 5\%$ uncertainties for neutron detection thresholds applied in the off-line analyses (Sec. IV).

IV. DATA ANALYSIS

The evaluation of the experimental data was performed by using our semiautomatic off-line program ANAL (Ref. 26) developed for use with the Kernforschungszentrum Karlsruhe central computer. The analysis began with the separation of neutron and γ events by consideration of two-dimensional arrays of pulse-height versus "pulse-shape discrimination" time. Excluding γ events from further analysis, the neutron events from the corresponding background runs were then subtracted. These data were subsequently sorted into suitable time-of-flight bins, and their energies calculated relativistically according to the time of occurrence of the prompt γ peak from the target. With the chosen neutron detection threshold and the flight path length, a single overlap in the neutron time-of-flight spectrum was admitted. Separation of the response due to high-energy neutrons from that due to low energy neutrons was achieved by extrapolation of the high energy pulse height response down to the bias level. The error associated with this procedure was small because of the largely different shapes of the corresponding pulse height distributions.

The contents of each time bin were integrated and divided by the neutron detection efficiency of the main neutron counter. The Monte Carlo code of Cecil *et al.*[27] was used to calculate the energy-dependent neutron detection efficiency of the counter. Calculations with this code provided good agreement with measured efficiencies for various hydrocarbon scintillators of largely different shapes and compositions for neutron energies from about 0.5 to 200 MeV and thresholds from 0.1 to 20 MeV.[27–30] There was, however, prior to our work,

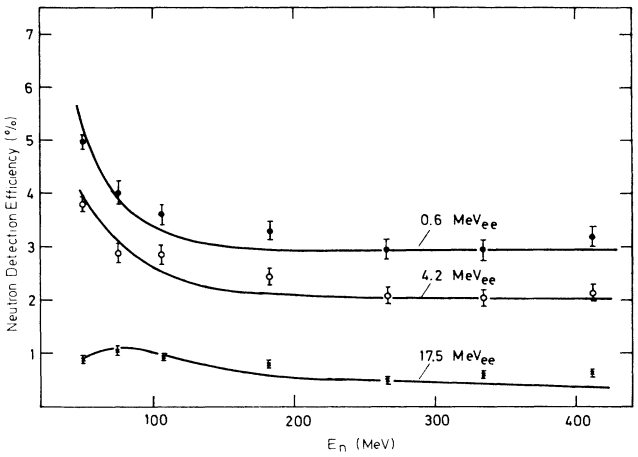

FIG. 5. Detector efficiency vs neutron energy for three different bias settings. The solid lines are the results from calculations using the Kernforschungszentrum Karlsruhe (KfK) version of the Monte Carlo code of Cecil *et al.* (Ref. 27). Our measured detector efficiencies from auxiliary associated-particle runs (Ref. 22) are also shown.

some doubt as to the accuracy of code predictions at higher energies, particularly in the range above the meson production thresholds. Therefore, the efficiency of our counter has been measured between 50 and 450 MeV in an auxiliary experiment employing the associated-particle method.[22] The measured and calculated efficiencies for three largely different thresholds of 0.6, 4.2, and 17.5 MeV_{ee} are shown in Fig. 5. It can be seen that there is good agreement between measurements and calculations, indicating that the code also predicts neutron detection efficiencies with good accuracy up to energies of more than 400 MeV. Additional confidence in the operation of the code at high energies came from the fact that the calculated shapes of pulse height spectra as a function of the incident neutron energy coincided favorably with the measurements. In the standard analyses of our data an off-line threshold of 0.62 MeV proton equivalent energy (MeV_{pe}) was used. For this threshold and a 5% uncertainty in threshold determination (see Sec. III) a total efficiency uncertainty of 8% was estimated for the lowest energy portions of the spectra. These uncertainties increased to 10% at maximum neutron energies. An overall uncertainty in efficiency determinations of 8–10% was also confirmed in auxiliary data analyses with different off-line thresholds between 0.6 and 2 MeV_{pe}.

The data were finally scaled by the solid angle subtended by the detector, the energy bin width, the dead time correction factor, and the number of incident protons to calculate the double differential neutron production cross sections. Finally, the double differential data were energy integrated over characteristic parts of the emission spectra to provide angular-dependent differential cross sections for the three laboratory angles of 30°, 90°, and 150°.

V. RESULTS AND DISCUSSION

A. Double differential cross sections

The results of the measurements are displayed in Figs. 6–8 in a double logarithmic representation. Table III summarizes our data for uranium.[31] Owing to the smooth energy dependence of the spectra, the experimental data have been binned in constant resolution intervals of 8%. Therefore, the energy uncertainties given in Table III refer to the off-line binning of the data, except for the highest bin numbers, where the experimental energy resolutions exceed the energy-bin intervals (cf. Table II). The angle uncertainties in the measurements are typically $\pm 0.5°$ and the angular acceptance was determined as 0.8×10^{-3} sr. Typical total uncertainties of $\sim 11\%$ (one standard deviation) have been estimated for the double differential neutron production cross sections. These estimates include contributions from counting statistics (0.1–3%), proton flux measurements (3%), neutron detection efficiencies (8–10%), target sample thicknesses (2%), and background determinations (3–10%).

The cross section curves in Figs. 6–8 are seen to be all very much alike, showing a flat distribution or a broad maximum below ~ 2 MeV, followed by a rapid fall to about 15 MeV. Then the spectrum continues with a different shape, exhibiting a more or less pronounced broad shoulder around ~ 100 MeV. The two different components in the spectra are attributed to evaporation neutrons dominating the range below ~ 20 MeV, and cascade neutrons governing th spectral shape above that energy. In general, the cascade neutrons originate from three different reaction mechanisms: (i) the quasielastic charge exchange (QEX) mechanisms, (ii) pion production and absorption reactions, and (iii) sequential inelastic scattering of nucleons produced in processes (i) and (ii).

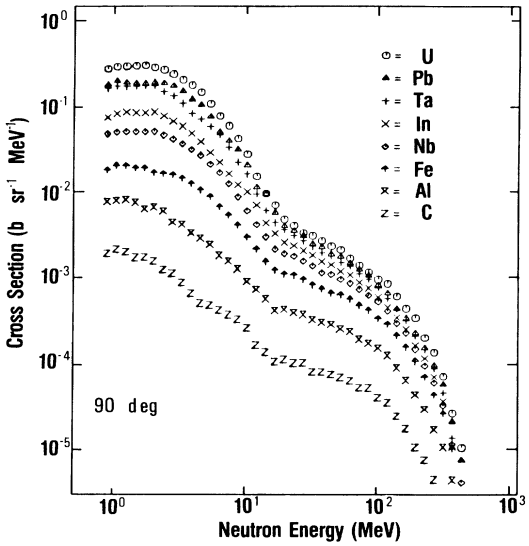

FIG. 7. Double differential neutron production cross sections for eight specified target materials at 90° laboratory angle.

Owing to the large observation angles and the moderate energy resolution above ~ 100 MeV in our experiments, particularly contributions of the primary processes (i) and (ii) are not seen as distinct separated peaks in any of the neutron spectra of Figs. 6–8. Small contributions are hidden in the high-energy tails of the individual cascade spectra. The absolute double differential cross sections are seen to increase with increasing target mass number over the entire energy range and for all neutron emission angles. Furthermore, the fraction of cascade neutrons in the total emission spectra increases with decreasing mass number for all three laboratory angles

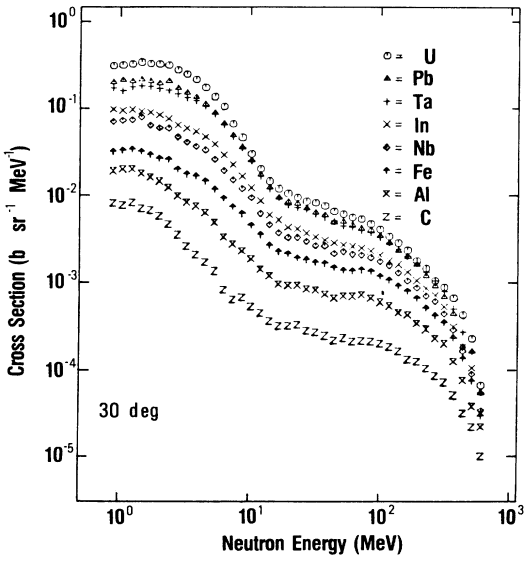

FIG. 6. Double differential neutron production cross sections for eight specified target materials at 30° laboratory angle.

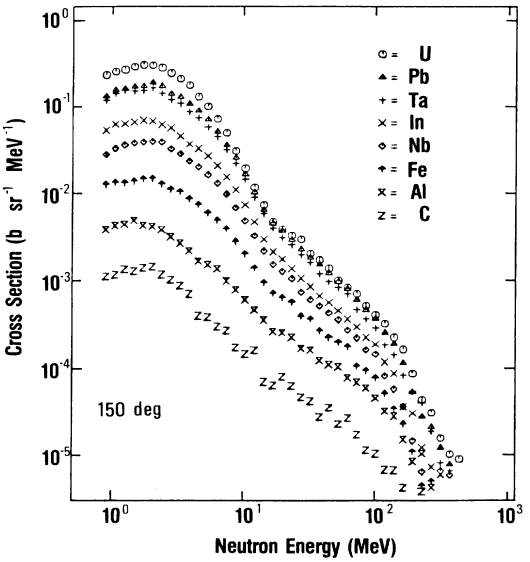

FIG. 8. Double differential neutron production cross sections for eight specified target elements at 150° laboratory angle.

(compare columns 4 and 5 of Table IV).

There exist presently only a few measurements for direct comparison with our double differential neutron production cross sections. Allowing for incident proton energies $450 \leq E_p \leq 800$ MeV and neutron emission angles of $\theta_n \geq 30°$, our data can be compared with the results of Wachter *et al.*[10] and the unpublished measurements of Howe[11] (see Figs. 9 and 10). As shown in Fig. 9, our 90° data agree satisfactorily with those of Howe over the entire spectral range for all commonly measured target elements except aluminum. (In the latter case the absolute cross sections of Howe are systemati-

TABLE III. Results of the present measurements for uranium. Results for all eight elements can be requested by reference to the report cited in Ref. 31 from the National Nuclear Data Center, Brookhaven National Laboratory, Upton, New York, 11973.

Bin no.	Energy (MeV)	30° $d^2\sigma/d\Omega dT_n$ (mb sr^{-1} MeV^{-1})	90° $d^2\sigma/d\Omega dT_n$ (mb sr^{-1} MeV^{-1})	150° $d^2\sigma/d\Omega dT_n$ (mb sr^{-1} MeV^{-1})
1	$0.899^{+0.08}_{-0.07}$	401.3±44.8	363.6±40.7	299.9±33.5
2	$1.057^{+0.09}_{-0.08}$	405.9±45.4	384.8±43.0	327.2±36.6
3	$1.244^{+0.11}_{-0.09}$	416.1±46.5	388.7±43.5	345.4±38.6
4	$1.463^{+0.13}_{-0.11}$	439.2±49.1	394.7±44.1	374.2±41.8
5	$1.722^{+0.15}_{-0.13}$	423.1±47.3	402.3±45.0	392.7±43.9
6	$2.026^{+0.18}_{-0.15}$	418.9±46.8	377.5±42.2	390.2±43.6
7	$2.383^{+0.21}_{-0.18}$	407.6±45.6	355.2±39.7	365.7±40.9
8	$2.804^{+0.24}_{-0.21}$	357.8±40.0	316.7±35.4	317.6±35.5
9	$3.299^{+0.29}_{-0.25}$	320.2±35.8	271.4±30.3	273.0±30.5
10	$3.881^{+0.34}_{-0.30}$	277.7±31.1	235.0±26.3	230.6±25.8
11	$4.566^{+0.40}_{-0.35}$	224.6±25.1	194.0±21.7	169.4±18.9
12	$5.37^{+0.46}_{-0.41}$	174.9±19.6	142.7±16.0	130.8±14.6
13	$6.32^{+0.55}_{-0.48}$	134.6±15.0	103.0±11.5	92.7±10.4
14	$7.44^{+0.64}_{-0.57}$	84.3±9.4	78.7±8.8	64.3±7.2
15	$8.75^{+0.76}_{-0.67}$	58.4±6.5	55.5±6.2	39.72±4.44
16	$10.29^{+0.89}_{-0.79}$	37.94±4.24	36.52±4.08	24.64±2.76
17	$12.11^{+1.05}_{-0.93}$	25.50±2.85	19.77±2.21	15.08±1.69
18	$14.24^{+1.23}_{-1.09}$	18.48±2.07	12.36±1.38	9.56±1.07
19	$16.76^{+1.45}_{-1.28}$	15.16±1.70	9.06±1.01	6.11±0.68
20	$19.72^{+1.71}_{-1.51}$	13.33±1.49	6.13±0.69	5.04±0.56
21	$23.20^{+2.01}_{-1.77}$	11.97±1.34	5.21±0.58	4.248±0.475
22	$27.29^{+2.36}_{-2.09}$	10.78±1.21	4.272±0.478	3.858±0.432
23	$32.11^{+2.78}_{-2.45}$	10.40±1.16	3.934±0.440	2.623±0.294
24	$37.77^{+3.27}_{-2.89}$	9.52±1.07	3.438±0.385	2.224±0.249
25	$44.43^{+3.85}_{-3.39}$	8.30±0.93	2.997±0.333	1.781±0.200
26	$52.3^{+4.6}_{-4.0}$	7.71±0.86	2.697±0.302	1.302±0.146
27	$61.5^{+5.9}_{-5.1}$	7.10±0.79	2.148±0.241	1.090±0.122
28	$72.4^{+7.6}_{-6.6}$	6.80±0.76	1.780±0.200	0.915±0.103
29	$85.1^{+9.9}_{-8.4}$	5.96±0.67	1.492±0.167	0.670±0.075
30	$100.1^{+12.9}_{-10.7}$	5.17±0.58	1.230±0.138	0.529±0.060
31	$117.8^{+16.9}_{-13.8}$	4.333±0.485	1.097±0.123	0.4199±0.0474
32	$138.6^{+22.2}_{-17.6}$	3.620±0.405	0.784±0.088	0.2921±0.0331
33	$163.0^{+29.2}_{-22.7}$	2.964±0.332	0.571±0.064	0.2136±0.0243
34	$191.8^{+38.8}_{-29.1}$	2.241±0.251	0.4427±0.0499	0.1139±0.0132
35	$225.6^{+51.8}_{-37.5}$	1.846±0.207	0.2632±0.0299	0.0566±0.0068
36	$265.4^{+69.7}_{-48.3}$	1.328±0.149	0.1799±0.0206	0.0399±0.0049
37	$312.2^{+94.8}_{-62.3}$	1.124±0.126	0.0947±0.110	0.0200±0.0026
38	$367.3^{+130.6}_{-80.6}$	0.845±0.095	0.0347±0.0043	0.0131±0.0019
39	$432.0^{+182.9}_{-104.2}$	0.542±0.061	0.0136±0.0019	0.0115±0.0017
40	$508.2^{+261.8}_{-134.9}$	0.2898±0.0329		
41	$597.8^{+386.2}_{-174.8}$	0.0846±0.0099		

cally lower by a factor of ~2 over the whole evaporation range.) All other small differences in spectral shapes and in absolute cross sections can, in principle, be understood on the basis of the different incident proton energies [585 MeV (this work) and 800 MeV (Ref. 11)] and laboratory emission angles [90° (this work) and 112° (Ref. 11)]. The comparison of our 30° results with those of Howe and of Wachter shows some other characteristic features (see Fig. 10). In the evaporation region there is also reasonable agreement with Howe's results (again except for Al), and any other small differences are explainable by the slightly different proton energies involved in the two measurements. In the cascade region there is a reasonable agreement between our data and those of Wachter *et al.*[10], whereas there is strong disagreement with the measurements of Ref. 11. The cross sections of Ref. 11 deviate increasingly with increasing energy, and are finally up to a factor of 5 higher than those from this work at 500 MeV. This discrepancy cannot, by far, be explained by differences in proton energies and emission angle, nor by differences in energy resolution: Even at 500 MeV maximum changes in spectral shape due to our moderate resolution have been estimated to be smaller than 15%. The low cross section values in the cascade region found in our work have been confirmed in a recent measurement at 800 MeV at Los Alamos National Laboratory (LANL). The preliminary

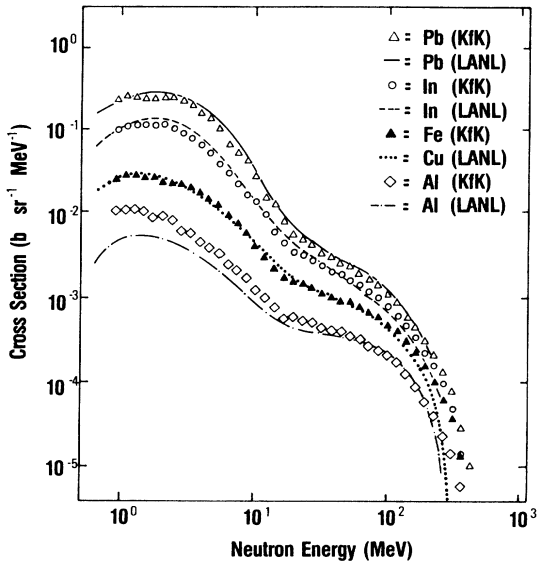

FIG. 9. Comparison of our measured double differential cross sections for neutron production at $T_p = 585$ MeV and $\theta_{lab} = 90°$ (KfK) with the unpublished results of Howe (LANL) (Ref. 11) at $T_p = 800$ MeV and $\theta_{lab} = 112°$. It can be seen that there is reasonable agreement between both data sets, except for aluminum below ~20 MeV (also see text).

TABLE IV. Summary of energy-integrated neutron production cross sections. For energy integration intervals, see text.

Target	$d\sigma_e/d\Omega$ (mb/sr)	$d\sigma_c/d\Omega$ (mb/sr)	$d\sigma_t/d\Omega$ (mb/sr)	$d\sigma_{HE}/d\Omega$ (mb/sr)
		150°		
U	1543±173	142.3±15.9	1685±188	64.4±7.2
Pb	1025±115	122.0±13.6	1147±128	53.5±6.0
Ta	878±98	98.2±11.0	976±109	43.4±4.8
In	396.5±44.3	56.3±6.3	452.8±50.6	24.7±2.8
Nb	243.4±27.2	42.4±4.7	285.8±31.9	18.6±2.1
Fe	93.4±10.4	23.5±2.6	116.9±13.1	10.8±1.2
Al	26.9±3.0	12.8±1.4	39.7±4.4	7.00±0.78
C	7.64±0.85	3.36±0.38	11.0±1.2	1.83±0.20
		90°		
U	1688±189	277.6±31.0	1966±220	162.4±18.1
Pb	1075±120	210.1±23.5	1285±144	121.1±15.5
Ta	937±105	205.0±22.9	1142±128	120.4±13.4
In	499.0±55.7	164.2±18.3	663±74	95.3±10.6
Nb	321.0±35.9	134.2±15.0	455.2±50.8	82.2±9.2
Fe	130.5±14.6	89.5±10.0	220.0±10.0	56.8±6.3
Al	41.7±4.7	37.2±4.2	78.9±8.8	24.0±2.7
C	9.88±1.10	10.1±1.1	19.9±2.2	6.52±0.73
		30°		
U	1961±219	1168±131	3129±351	861±96
Pb	1299±145	927±104	2226±249	693±77
Ta	1174±131	949±106	2123±237	716±80
In	557±62	591±66	1148±128	458±51.2
Nb	405.5±45.2	490.8±54.8	896±100	384.1±42.9
Fe	192.1±21.4	345.4±38.6	537±60	278.3±31.1
Al	88.9±9.9	178.1±19.9	267.0±29.8	146.6±16.4
C	29.9±3.3	62.8±7.0	92.7±10.4	52.3±5.8

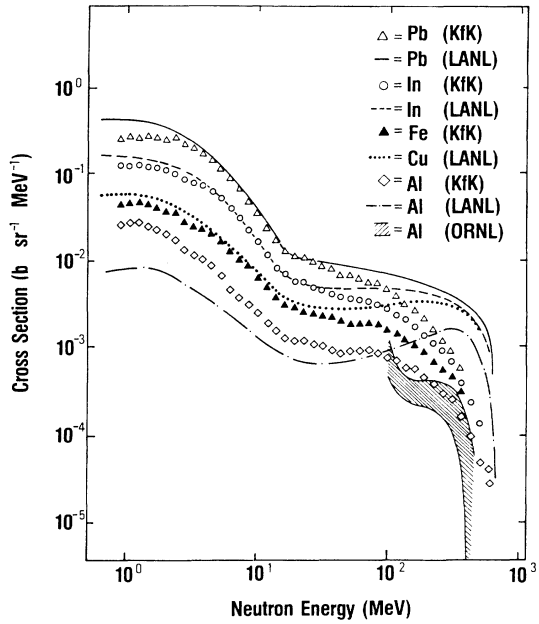

FIG. 10. Comparison of measured double differential cross sections for the production of neutrons at $T_p = 585$ MeV and $\theta_{lab} = 30°$ with the results of Wachter *et al.* Oak Ridge National Laboratory (ORNL) (Ref. 11) at $T_p = 450$ MeV and of Howe (LANL) (Ref. 11) at $T_p = 800$ MeV and $\theta_{lab} = 30°$. There is reasonable agreement between our and Howe's data below ~20 MeV and our and Wachter's results above 120 MeV. For large discrepancies see text.

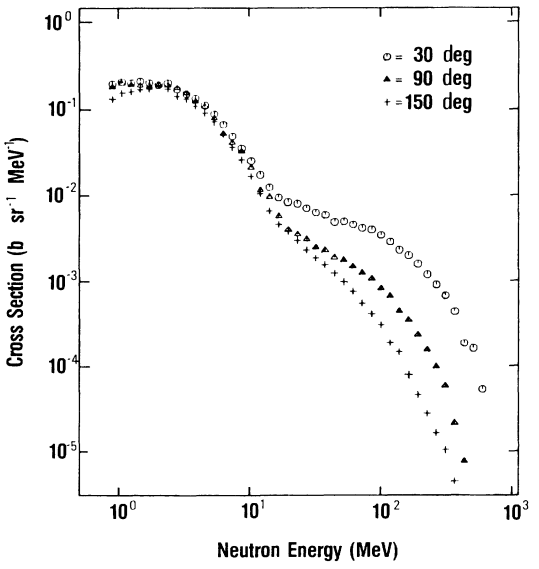

FIG. 11. Differential cross sections vs neutron energy for a typical heavy mass target nucleus (lead) as a function of laboratory angle. While below about 15 MeV the data for all three angles almost coincide, there is a strong forward peaking above that energy, increasing rapidly with increasing neutron energy.

nary 30° data reported for C, Al, Pb, and U by Meier *et al.*[32] agree with our results within ~20% over the whole commonly measured energy range from 5 to 500 MeV.

In Fig. 11 the double differential data for a typical heavy element target (lead) are shown for the three laboratory angles of 30°, 90°, and 150°. It can be seen that below about 15 MeV the cross sections for all three angles widely coincide, indicating an almost isotropic neutron emission. A closer inspection of these data reveals, however, two small but systematic differences: (i) a slight decrease of absolute cross sections over the entire evaporation spectrum with increasing emission angle, and (ii) a systematic change in spectral shape below about 2 MeV. In Fig. 11 the latter change appears mainly between the two low-angle and the 150° data. But the decrease in cross section with angle by 17% at 0.9 MeV is significantly larger than the estimated uncertainty in efficiency of 8% close to the software threshold. This behavior, which becomes more pronounced for the lighter elements, is at least partly due to the display of the data in the laboratory system instead of the zero linear momentum (ZLM) system. Increased forward neutron emission in the laboratory system results from the motion of the origin of the ZLM coordinate system for the incident proton and the target nucleus. In addition, this motion in the laboratory system causes a Doppler-type shift in the energy distribution which noticeably alters the low energy tails of the spectra qualitatively in the observed manner.

In contrast to the evaporation region, the neutron production cross sections in the cascade region are strongly angular dependent, and forward peaking is evident, as expected from theory. While the high-energy cross sections around 20 MeV are still of about the same order for all three angles, the cascade component tails off rapidly, increasing with increasing emission angle.

The general features of the angular dependent cross sections are very similar for all other target elements, except for aluminum and carbon in the evaporation region. For these two light elements the evaporation model is less adequate, and the absolute cross sections and the spectral shapes also vary considerably with emission angle, showing the larger cross section values at forward angles.

B. Energy-integrated cross sections

A better systematic comparison with other experimental results can be obtained by integrating our double differential cross sections over appropriate neutron energy intervals. Table IV gives the results for a few of such energy integrations. The cross sections $d\sigma/d\Omega_e$ (integrated over the evaporation range from 0.9 to 20 MeV), $d\sigma/d\Omega_c$ (integrated over the cascade region from 20 to 585 MeV), and the total cross sections $d\sigma/d\Omega_t$ (integrated over the total measured range) are listed together with the high-energy cross sections $d\sigma/d\Omega_{HE}$ (covering the neutron energy range from 50 MeV to maximum). The high-energy cross sections $d\sigma/d\Omega_{HE}$ are plotted in Fig. 12 versus target mass as a function of

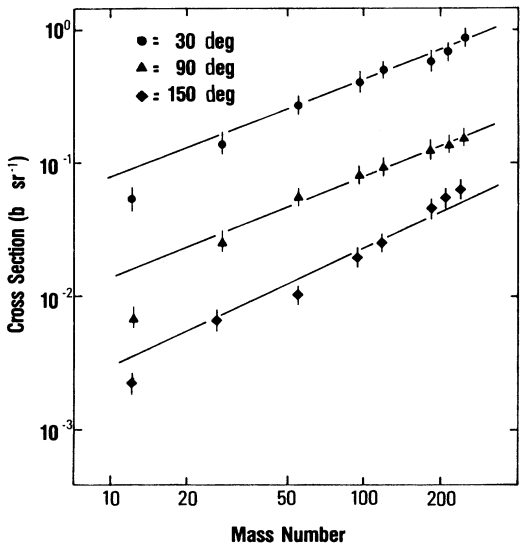

FIG. 12. Differential (p,n') cross sections $d\sigma/d\Omega_{HE}$ (integrated over the high-energy range from 50 MeV to maximum) vs target mass number. The solid lines are least-squares fits through the measured data points excluding the results for carbon (see text).

TABLE V. Parameters, parameter uncertainties (1σ), and parameter correlation factors used to fit the cross sections in Fig. 12 by $d\sigma/d\Omega_{HE}=aA^b$. The parameter a is in units of mb/sr; the parameter b is dimensionless.

Angle (deg)	Parameter a	Parameter b	Correlation factor
30	11.38 ±2.18	0.76±0.04	0.99
90	1.92 ±0.35	0.80±0.04	0.99
150	0.165±0.036	1.02±0.05	0.99

the neutron emission angle. It can be seen that the data points for each angle lie very closely along a straight line on a double-logarithmic plot. Adopting the procedure applied in the empirical description of some high-energy (p,p') data,[8,9] an A dependence of the form $d\sigma/d\Omega=aA^b$, with a and b being constants, was assumed and fitted to the data by the least-squares method. In the fitting procedure, however, the data of carbon have been excluded, since these are systematically low for all three angles. The corresponding results of the fits are shown in Fig. 12 as solid lines through the data points. The pa-

TABLE VI. Comparison of measured (p,p') and (p,n') cross sections. Except for the 450 MeV data, all other results are energy integrated from ~50 MeV to maximum energy.

Target	Proton energy (MeV)	Energy-integrated cross sections (mb/sr) at angle: 30° (p,p')	30° (p,n')	45° (p,p')	45° (p,n')	90° (p,n')	112° (p,n')
C	450[a]	59.4±7.4[f]	22.1±4.2[f]	22.4±2.2[f]			
	558[b]	80.4±5.6					
	585[c]		52.3±5.8			6.5±0.7	
	660[d]	114.3±6.0					
Al	450[a]	94.2±13.5[f]	73.7±22.1[f]	36.6±3.6[f]			
	558[b]	146.3±10.2					
	585[c]		146.6±16.4			24.0±2.7	
	800[e]				203±20.5		18±2.7
Fe	558[b]	204.6±14.3					
	585[c]		278.3±31.1			56.8±6.3	
Cu	558[b]	239.4±16.7					
	660[d]	335.7±11.0					
	800[e]				335±33.5		38±5.7
In	585[c]		458.3±51.2			95.3±10.6	
	800[e]				543±81		134±13
Pb	558[b]	447.6±31.3					
	585[c]		693±77			121±15.5	
	800[e]				830±124		164±25
U	585[c]		861±96			162.4±18.1	
	660[d]	592±30					
	800[e]				840±126		240±36

[a]J. W. Wachter *et al.*, Ref. 10.
[b]S. M. Beck and C. A. Powell, Ref. 8.
[c]This work.
[d]L. S. Azhgirey *et al.*, Ref. 9.
[e]S. D. Howe, Ref. 11.
[f]Energy integrated from 120 MeV to maximum energy.

rameters a and b obtained for the three emission angles are summarized in Table V. While the parameter a varies strongly with angle, the parameter b increases smoothly with angle from 0.76 to 1.02. The value of $b=0.76$ for the 30° cross sections is in reasonable agreement with the $A^{2/3}$ dependence measured for the corresponding (p,p′) data at this emission angle.[8]

In Table VI the high-energy cross sections of this experiment are compared with (p,n′) and (p,p′) data on the same or similar targets measured at other laboratories for proton energies between 450 and 800 MeV. Due to the lack of many large-angle (p,n′) data, also the unpublished data of Howe taken for 45° and 112° laboratory angles and energy integrated over the high-energy range have been included in the table. (The 30° data which deviate from the other measurements by large factors have been neglected in this comparison.) The cross sections from our work are in good qualitative agreement with previous results: From the previous (p,p′) and (p,n′) data measured in different laboratories, it can be seen that the high-energy cross sections for identical targets and emission angles increase slowly with increasing proton bombarding energy. The corresponding increase is less than a factor of 2 over the range from 450 to 800 MeV, as can be judged from the extrapolated 30° cross sections for Al, C, and Be given in Refs. 8–10. From the 30° data of Ref. 10, it appears also that the magnitude of (p,p′) and (p,n′) cross sections on the same nucleus is about the same as predicted from intranuclear model calculations above the meson-production threshold (Table II of Ref. 6). This is different for low proton energies of 90 MeV, where nucleon-nucleon scattering is dominant and proton-to-neutron ratios of ~ 2 were found.[33] On this basis, the slight increase of (p,n′)-to-(p,p′) ratios with mass for the 585 and 558 MeV data at 30° mainly reflects the increasing ratio of neutrons to protons in the target nuclei.

VI. CONCLUSIONS

In conclusion, we have determined absolute differential neutron production cross sections at 585 MeV proton bombarding energy over a broad range of target masses, secondary energies, and emission angles with a total accuracy of 10–15 %. These data represent a large consistent set of experimental data useful for detailed comparisons with present theoretical predictions. All of the energy-dependent cross sections clearly reveal a two-component structure with contributions from evaporation processes and intranuclear cascade reactions. For heavy and medium weight target nuclei the cross sections in the evaporation region are qualitatively indicative of an isotropic angular distribution in the ZLM system. The cross section data in the cascade region exhibit a strongly forward-peaked angular distribution. The fraction of cascade neutrons increases rapidly with decreasing neutron emission angle and decreasing target mass number. It is the motivation of the following paper (Ref. 19) to investigate to what extent the experimentally observed cross sections and phenomena can be quantitatively described by the intranuclear cascade evaporation models used in modern high-energy nucleon-meson transport codes.

ACKNOWLEDGMENTS

The authors at Kernforschungszentrum Karlsruhe would like to thank Prof. A. Citron for helpful discussions and for his on-going interest in this work. They are also indepted to Prof. W. Kluge and his group members, in particular Dr. H. Matthäy and Dr. U. Klein, for providing invaluable support during the initial phase of the experimental program. The help of the SIN staff, especially Dr. W. Fischer and Dr. C. Tschalär, is also gratefully acknowledged.

*Present address: Electrotechnical Laboratory, 114 Umezono, Ibaraki, Japan.

†Permanent address: Institut für Neutronenphysik und Reaktortechnik, Kernforschungszentrum Karlsruhe, Karlsruhe, Federal Republic of Germany.

[1]G. S. Bauer, H. Sebening, J. E. Vetter, and H. Willax, Joint Kernforschungsanlage Jülich and Kernforschungszentrum Karlsruhe Report Jül-Spez-113/KfK 3175, 1981.

[2]S. Cierjacks, M. T. Rainbow, M. T. Swinhoe, and L. Buth, Kernforschungszentrum Karlsruhe Report KfK 3097B, 1980.

[3]N. Metropolis, R. Bivins, M. Storm, J. M. Miller, G. Friedlander, and A. Turkevich, Phys. Rev. **110**, 185 (1958).

[4]K. Chen, Z. Fraenkel, G. Friedlander, J. R. Grover, J. M. Miller, and Y. Shimamoto, Phys. Rev. **166**, 949 (1968).

[5]K. Chen, G. Friedlander, G. D. Harp, and J. M. Miller, Phys. Rev. C **4**, 2234 (1971).

[6]H. W. Bertini, Phys. Rev. **131**, 1801 (1963); **138**, AB2(E) (1965); **188**, 1711 (1969).

[7]R. G. Alsmiller, Jr., J. W. Wachter, and H. S. Moran, Nucl. Sci. Eng. **36**, 291 (1969).

[8]S. M. Beck and C. A. Powell, NASA Technical Note NASA-TN-8119, 1976.

[9]L. S. Azhgirey, I. K. Vzorow, V. P. Zrelov, M. G. Meshcheryakov, B. S. Neganov, R. M. Ryndin, and A. F. Shabudin, Nucl. Phys. **13**, 258 (1959).

[10]J. W. Wachter, W. A. Gibson, and W. R. Burrus, Phys. Rev. C **6**, 1496 (1972).

[11]S. D. Howe, Ph.D thesis, Kansas State University, 1980.

[12]R. Madey and F. M. Waterman, Phys. Rev. C **8**, 2414 (1973).

[13]C. G. Cassapakis, H. C. Bryant, B. D. Dieterle, C. P. Leavitt, D. M. Wolfe, B. E. Bonner, J. E. Simmons, C. W. Bjork, P. J. Riley, M. L. Evans, G. Glass, J. C. Hiebert, M. Jain, R. A. Kenefick, L. C. Northcliffe, and D. W. Werren, Phys. Lett. **63B**, 35 (1976).

[14]B. E. Bonner, J. E. Simmons, C. R. Newsom, P. J. Riley, G. Glass, J. C. Hiebert, M. Jain, and L. C. Northcliffe, Phys. Rev. C **18**, 1418 (1978).

[15]J. S. Fraser, J. S. Hewitt, and J. Walker, Phys. Can. L **2**, 62 (1966).
[16]R. R. Fullwood, J. D. Cramer, R. A. Haarman, R. P. Forrest, and R. G. Schrandt, Los Alamos Scientific Laboratory Report LA-4789, 1972.
[17]F. M. Waterman and R. Madey, Phys. Rev. C **8**, 2419 (1973).
[18]J. W. Wachter, R. T. Santoro, T. A. Love, and W. Zobel, Bull Am. Phys. Soc. **18**, 118 (1973).
[19]D. Filges, P. Cloth, T. W. Armstrong, S. Cierjacks, Y. Hino, F. Raupp, and L. Buth, the following paper, Phys. Rev. C **36**, 1988 (1987).
[20]P. Cloth, D. Filges, G. Sterzenbach, T. W. Armstrong, and B. L. Colborn, Kernforschungsanlage Jülich Report Jül-Spez-196, 1983.
[21]M. Ahmed, Nucl. Instrum. Methods **143**, 255 (1977).
[22]S. Cierjacks, M. T. Swinhoe, L. Buth, S. D. Howe, F. Raupp, H. Schmitt, and L. Lehmann, Nucl. Instrum. Methods **192**, 407 (1982).
[23]M. Daum, SIN Report TM-09-45 1976 (unpublished).
[24]G. H. Eaton and F. Pozar, SIN Report TM-33-02, 1975 (unpublished).
[25]P. Cloth, private communication.
[26]M. T. Rainbow and S. Cierjacks, A Computer Program System for the Off-line Analysis of 4-Parameter Neutron and Charged-Particle Time-of-Flight Data, Internal KfK Note, 1981 (unpublished).
[27]R. A. Cecil, B. D. Anderson, and R. Madey, Nucl. Instrum. Methods **161**, 439 (1979).
[28]S. Cierjacks, T. Petković, H. Ullrich, D. Gotta, S. Ljungfelt, N. Simicević, M. Izycki, P. Weber, and H.-J. Weyer, Nucl. Instrum. Methods A **238**, 354 (1985).
[29]W. J. McDonald, H. Anderson, L. Antonuk, W. K. Dawson, D. A. Hutcheon, P. Kitching, C. A. Miller, and D. M. Sheppard, Nucl. Instrum. Methods **166**, 467 (1979).
[30]P. T. Debevec, G. L. Moake, and P. A. Quin, Nucl. Instrum. Methods **166**, 467 (1979).
[31]D. Filges, S. Cierjacks, Y. Hino, T. W. Armstrong, and P. Cloth, Joint Kernforschungsanlage Jülich and Kernforschungszentrum Karlsruhe Report Jül-1960/KfK 3779, 1984.
[32]M. M. Meier, D. Holtkamp, G. Morgan, H. Robinson, G. Russel, R. Whitaker, W. Amian, and N. Paul, Radiat. Effects **96**, 467 (1986).
[33]A. M. Kalend, B. D. Anderson, A. R. Baldwin, R. Madey, J. W. Watson, C. C. Chang, H. D. Holmgren, R. W. Koontz, J. R. Wu, and H. Machner, Phys. Rev. C **28**, 105 (1983).